Flow, Turbulence and Combustion
https://doi.org/10.1007/s10494-021-00269-8

Turbulence-Driven Blowout Instabilities of Premixed Bluff-Body Flames

Anthony J. Morales[1] · Tommy Genova Jr.[1] · Jonathan Reyes[1] · Isaac Boxx[2] · Kareem A. Ahmed[1]

Received: 17 November 2020 / Accepted: 28 April 2021

Abstract
Bluff-body flame instabilities are experimentally investigated under varying turbulence conditions during lean blowout. For all turbulence conditions, the blowout process is induced through a temporal reduction of the fuel flow rate to capture the flame-flow dynamics approaching blowout. Simultaneous high-speed particle image velocimetry (PIV), stereoscopic PIV, and C_2*/CH* chemiluminescence imaging are employed, along with an independent CH* imaging system, to capture flame-flow instabilities. Proper orthogonal decomposition (POD) and dynamic mode decomposition (DMD) techniques are used to identify prominent flame oscillations and evaluate recurring spatiotemporal modes during blowout. The results reveal that the dominant flame oscillations and wrinkling characteristics are directly dependent on the turbulence conditions in the combustor. Specifically, the flame-flow oscillations are strongly coupled with the integral length scales, which were able to collapse the oscillation frequencies to a unified value. The turbulence-driven flame-flow oscillations are shown to largely impact the magnitude, temporal evolution, and oscillatory behavior of the flame strain rate. As the turbulence intensity is increased, the oscillation of the flame strain rate increases in frequency, making it more likely for localized extinctions to occur. Additionally, the magnitude of the flame strain rate increases at high turbulence intensities and accelerates the lean blowout process.

Keywords Turbulent premixed flames · Bluff-body · Flame extinction

1 Introduction

Lean combustion processes are desired in propulsion and energy production technologies to improve engine efficiency and minimize pollutant emissions (Candel 2002). However, lean combustion processes are highly sensitive to hydrodynamic instabilities, as well as

✉ Kareem A. Ahmed
Kareem.Ahmed@ucf.edu

[1] Department of Mechanical and Aerospace Engineering, Center for Advanced Turbomachinery and Energy Research, University of Central Florida, Orlando, FL 32816, USA

[2] Institute of Combustion Technology of the German Aerospace Center, Deutsches Zentrum für Luft-und Raumfahrt (DLR), Institute für Verbrennungstechnik, Stuttgart, Germany

disturbances that may arise from minor or unintentional variations in the equivalence ratio or turbulence conditions (Markovich et al. 2014). These disturbances may lead to localized extinctions along the flame front or global flame blowout. Therefore, further investigations of lean blowout are desired, with particular emphasis on the influence of turbulence on flame-flow instabilities and transient blowout physics (Shanbhogue et al. 2009).

Bluff-bodies are commonly used to stabilize flames within many combustion technologies such as ramjet engines or afterburners (Lovett et al. 2004). The bluff-body provides a sheltered low-velocity recirculation zone surrounded by shear layers to stabilize flames (Longwell et al. 1953a, b). Inflow reactants are continually ignited in the shear layer regions and entrained into the recirculation zone. Hot recirculating products then convect back into the upstream shear layer regions and ignite fresh inflowing mixture, providing stable flames. Although the stabilization process is well defined, there are finite limits in which flames can be stabilized. The stability limits are a function of many physical parameters, including equivalence ratio and turbulence (Ozawa 1971; Herbert 1960; Ballal and Lefebvre 1979). If the operating conditions are pushed beyond stability limits, flame blowout will occur and the combustion process will terminate (Zukoski and Marble 1956). For instance, experimental investigations have demonstrated that increasing the freestream turbulence intensity will shrink the stability limits for bluff-body flames, and blowout will occur at higher equivalence ratios (Ballal and Lefebvre 1979; Roy Chowdhury and Cetegen 2017). Thus, it remains of interest to understand how turbulence and hydrodynamics influence the flame instabilities.

To improve the operational envelope of combustion systems, many research studies have focused on identifying the physical processes that drive lean blowout. Within literature, lean blowout has been described in two distinct stages (Shanbhogue et al. 2009; Nair and Lieuwin 2007). The first stage consist of localized extinctions along the flame front, which occur at lean conditions due to a decreased flame speed and decreased density ratio between reactants and products. The decreased flame speed causes the flame front to reside closer to the shear layer vorticity regions (Chaudhuri et al. 2010), while the decreased density ratio diminishes the production of baroclinic and dilatation vorticity and allows the shear layer vorticity to increase in magnitude (Morales et al. 2019, 2020a). Combined, these effects lead to flame and shear layer interactions, which invoke high strain rate magnitudes along the flame front (Chaudhuri et al. 2010; Tuttle et al. 2013). If the premixed flame experiences excessive strain rates which are larger than the extinction strain rate for a sufficiently long period (Sardi and Whitelaw 1999; Sardi et al. 2000), localized extinctions will occur and flame holes form Shanbhogue et al. (2009), Nair and Lieuwin (2007). The intense straining processes that induce localized extinctions are analogous with Damköhler (Da) number descriptions of lean blowout, where the Damköhler number represents the ratio of the fluid mechanical timescales to the chemical timescales ($Da = \tau_{flow}/\tau_{chem}$). In this case, the high flame straining and localized extinctions are associated with small (or fast) fluidic timescales, and low Damköhler numbers. Although the onset of local extinction and formation of flame holes does not necessarily indicate that global blowout will occur, any further decrease in the equivalence ratio can induce the onset of the of the blowout process. These general physical descriptions of lean blowout hold also true for non-premixed flame configurations (Masri et al. 1990); however, non-premixed flames will have additional considerations, such as a non-uniform mixture composition (Lignell et al. 2011), which will influence the balance of fluidic and chemical timescales and the onset of localized extinction.

The second stage of blowout is associated with a large-scale variation of flame and flow dynamics in the bluff-body wake. In this stage, the flame structure transitions from a

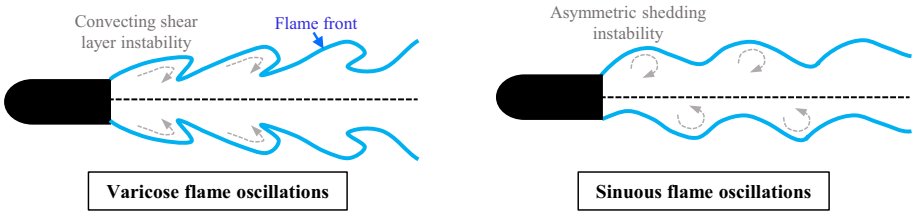

Fig. 1 Schematic of varicose and sinuous flame oscillation modes, which are representative of the first and second stages of the blowout process, respectively (Shanbhogue et al. 2009; Emerson and O'connor 2012)

varicose mode (symmetric across the bluff-body centerline) to a sinuous mode (Emerson and O'connor, J., Juniper, M., Lieuwen, T. 2012), as depicted in Fig. 1. For the sinuous mode, the flame boundary resembles the Bénard von-Kármán (BVK) instability associated with nonreacting flows (Nair and Lieuwin 2007; Erickson and Soteriou 2011). The topological alteration of the flame is linked with a transition from a convective shear layer instability to an absolute instability (which is more easily destabilized) in the bluff-body wake (Emerson and O'connor 2012). The transition to an absolute instability causes the flow field oscillation frequencies to decrease with the equivalence ratio (Morales et al. 2019, 2020a), until global blowout occurs and the wake locks into the BVK instability (Emerson and O'connor 2012). Thus, the characteristics of the flame are highly sensitive to hydrodynamic instabilities near blowout.

This goal of this paper is to expand upon recent experimental work and characterize the influence of turbulence on: (1) flame and flow field instabilities at lean conditions, and (2) the subsequent impacts on the flame strain rate and the lean blowout process. The research is conducted with a turbulent bluff-body combustor paired with high-speed PIV and chemiluminescence diagnostics. Similar to previous experiments, the analysis is focused on characterizing the temporal instabilities during the lean blowout process, but also includes data from stable reacting conditions to validate the results. The results demonstrate that the flame, strain, and flow instabilities are dependent on turbulent length scales, while turbulent velocity scales primarily influence the magnitude of the flame strain rate. Ultimately, this knowledge provides a more comprehensive understanding of turbulent flame-flow instabilities and provide additional insights of lean blowout physics.

2 Experiment and Diagnostics

2.1 Experimental Facility

The experimental facility used in this study is the same facility detailed by Morales et al. (2020a), and consist of a flow conditioning plenum which exhausts into a combustion test section. A full schematic of the experimental facility, including the flow control network, are detailed in previous work (Morales et al. 2020a); however, the experiment is also described below for completeness.

Propane and air are injected well upstream of the flow conditioning plenum to ensure reactants are fully mixed prior to entering test section. The test section is shown in Fig. 2a, and includes a turbulence generator, a bluff-body flame stabilizer, and an optical viewing region. The bluff-body is shown in Fig. 2b. The height of the bluff-body

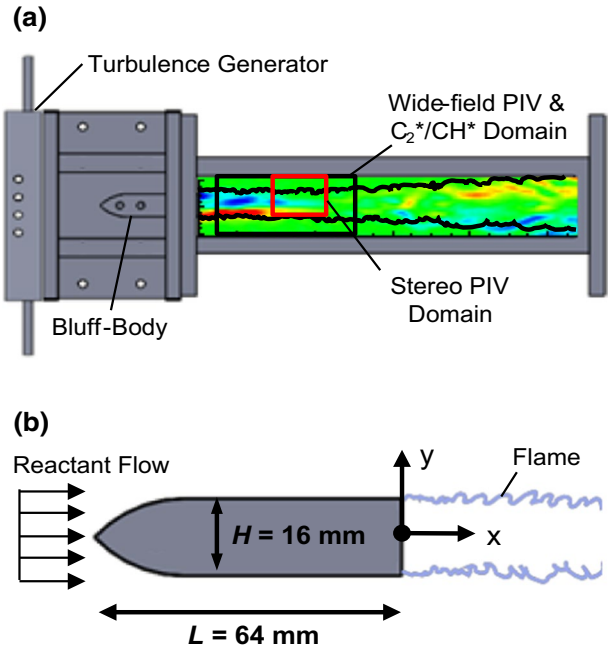

Fig. 2 Combustion test section. **a** Test section components with investigation domains and **b** bluff-body flame stabilizer and dimensions

is 16 mm, providing a blockage ratio of ≈ 35%. The optical viewing region is rectangular with a length, height, and depth (into the page) of 260, 45, and 127 mm, respectively. All test section walls, except for the top wall, are recessed and fitted with fused silica windows that provide 95% transmissivity for wavelengths between 250–700 nm. The upper test section wall is made of steel which was painted black to minimize light reflections within the optical viewing region.

To study the effects of turbulence on lean blowout physics, a turbulence generator is used to modify the freestream turbulence in the combustor. The design is shown in Fig. 3 and combines a static grid with impinging premixed supersonic jets. The static grid contains a set of hollow cylindrical tubes that make up a rectangular mesh. There are 12 tubes in total, each with an inner and outer diameter of 4 and 4.4 mm, respectively. Eight of the tubes are oriented vertically and the remaining four are oriented horizontal to create the rectangular mesh. The vertical and horizontal spacing between adjacent tubes is 11.3 and 15.9 mm, respectively, as shown in Fig. 3. The tube spacing produces a blockage ratio of 56% with respect to the cross-sectional area.

Fluidic jet impingement can also be implemented by injecting propane and air (at $\Phi = 0.7$) into both ends of each tube. The mixture is then ejected through 0.8 mm impingement holes drilled along the length of each tube. The impingement holes are oriented orthogonal to the bulk flow and evenly spaced in the horizontal and vertical directions, as shown in Fig. 3. At high flow rates, the mixture will choke at the impinging holes, creating supersonic under-expanded premixed jet plumes. The supersonic jet structures are verified by schlieren imaging, which is also provided in Fig. 3. The impinging jets interact with the premixed freestream flow to induce small-scale, high-intensity turbulence. Additional details of the different turbulence conditions are provided in Sect. 2.4.

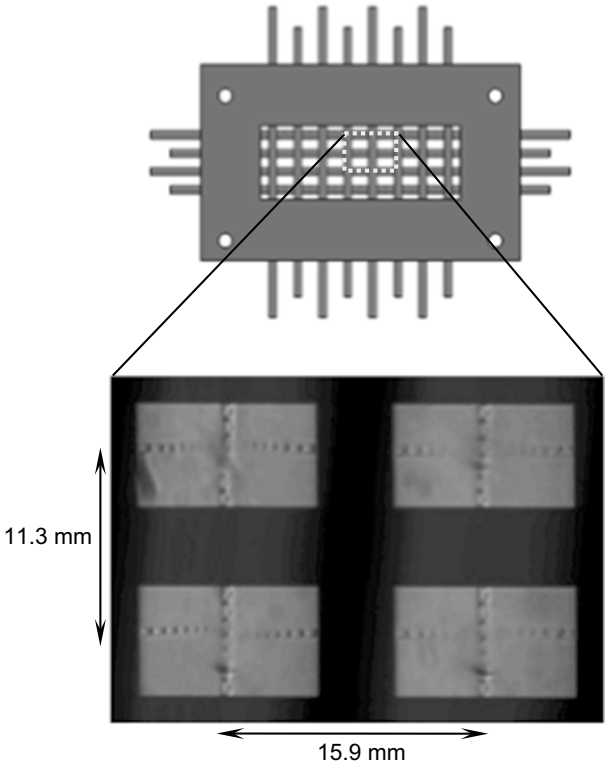

Fig. 3 Turbulence generator and supersonic impinging propane-air jet orientation. The bulk flow into the test section is orthogonal to the page

2.2 Flow control systems and blowout methodology

High pressure air at 300 K is ducted into the flow conditioning plenum upstream of the combustion test section. The air flow rate is modulated with a DM4500 electropneumatic JFlow valve. The air flow is measured with a Preso CV-300–65 Venturi flowmeter and a Dwyer 626 pressure transducer. The measurement system is connected to a feedback loop within LabVIEW software, which autonomously controls the position of the JFlow valve and allows for a desired velocity within the test section to be maintained during experimentation.

Gaseous propane (C_3H_8) at 300 K is injected upstream of the flow conditioning plenum to ensure a premixed mixture reaches the combustion test section. The propane flow rate is controlled with an in-line regulator, a Burkert type 5282 solenoid valve, and a Dwyer RMC-122 rotameter. The flow network results in an uncertainty in the fuel flow rate of $\pm 5 \times 10^{-4}$ kg/s.

For all experiments, the premixed propane-air mixture is fed into the test section at a lean equivalence ratio of $\Phi = 0.7$ and ignited. The lean flame is sustained for a short duration of ~ 2 s prior to the initiation of the blowout process to prevent the bluff-body from preheating. Lean blowout is induced using a similar method as Chaudhuri et al. (2010), Tuttle et al. (2013), and Kariuki et al. (2012), where the fuel flow into the reactant mixture is decreased through time. This method is particularly advantageous over alternative methods, such as fixing the equivalence ratio to a value near the lean blowout limit, because the

blowout equivalence ratio is expected to change with varying turbulence intensities (Ballal and Lefebvre 1979; Chowdhury and Cetegen 2018). This would inherently bias the stability characteristics (Ballal and Lefebvre 1979; Chaudhuri et al. 2011), turbulence-flame interactions (Lipatnikov et al. 2014; Dopazo et al. 2017; Chakraborty et al. 2016), and exothermic effects on the flow field (Geikie et al. 2017). Thus, identifying the source of the flame instabilities would require an effort to decouple the effects of turbulence from the effects of the equivalence ratio. Instead, the fuel reduction technique employed here provides an unbiased approach, where the effects of turbulence can be directly isolated. The temporal fuel reduction is accomplished using a timed control system that closes a solenoid valve in the propane injection line. The response time of the solenoid value is 200 ms (0.2 s), which ensures that the total duration of the lean blowout process is less than 200 ms for all turbulence conditions, and the blowout process can occur repeatably within the experimental duration of 250 ms. The total duration of the lean blowout process is approximately 12–200 times longer than the chemical and flow time scales and is sufficient for capturing the transient flame-flow physics (Shanbhogue et al. 2009). It is also noteworthy that the temporal decrease in the fuel flow rate does not impact the bulk flow rate through the combustor. Since the reaction is initially stabilized at a lean condition of $\Phi = 0.7$, the change in equivalence ratio between the initial state and the point where the flame blows out is minimal ($\Delta\Phi \leq 0.2$ for all cases explored here). This corresponds to a *maximum* change in the freestream velocity of 0.7 m/s, which is less than 3% of the mean freestream velocity of 25 m/s.

2.3 High-Speed Diagnostics

The experiment and diagnostic systems used in this study have been described by the authors in previous literature (Morales et al. 2020a), and a brief summary is provided here for completeness. Three simultaneous high-speed diagnostics are implemented to capture the transient blowout process: (1) a wide-field, two-component PIV system, (2) a high-resolution, three-component stereoscopic PIV system, and (3) a line-of-sight C_2*/CH* chemiluminescence imaging system. Additional experimental trials were executed under equivalent conditions to accommodate an independent CH* imaging system, which was used for POD and DMD analysis. A summary of the diagnostics is provided below, and an overview of the optical setup is presented within Fig. 4.

2.3.1 PIV Systems

For both the wide-field and stereoscopic PIV systems, a pressurized swirl seeder is used to inject 150 nm Al_2O_3 particles into the reactant mixture far upstream of the bluff-body. The particles are illuminated with a 532 nm dual-head ND:YAG laser (LDP-200MQG Dual), pulsing at a 20 kHz repetition rate. The laser is formed into a sheet using cylindrical and spherical lenses and directed upward into the test section from below using a mirror as depicted within Fig. 4.

In the wide-field PIV system, sequential PIV images are collected on a high-speed CMOS camera (Photron SA1.1) equipped with a 50 mm focal length, *f/1.2* lens. The camera is mounted perpendicular to the bluff-body combustor (Fig. 4) and is focused on a domain of 64 × 64 mm between $0.55 \leq x/H \leq 4.75$, as shown in Fig. 2a. Sequential PIV images are acquired at 20 kHz onto a sensor comprised of 512 × 512 pixels, giving a pixel resolution of 125 μm/pixel. Velocity vector fields are obtained by processing the images in

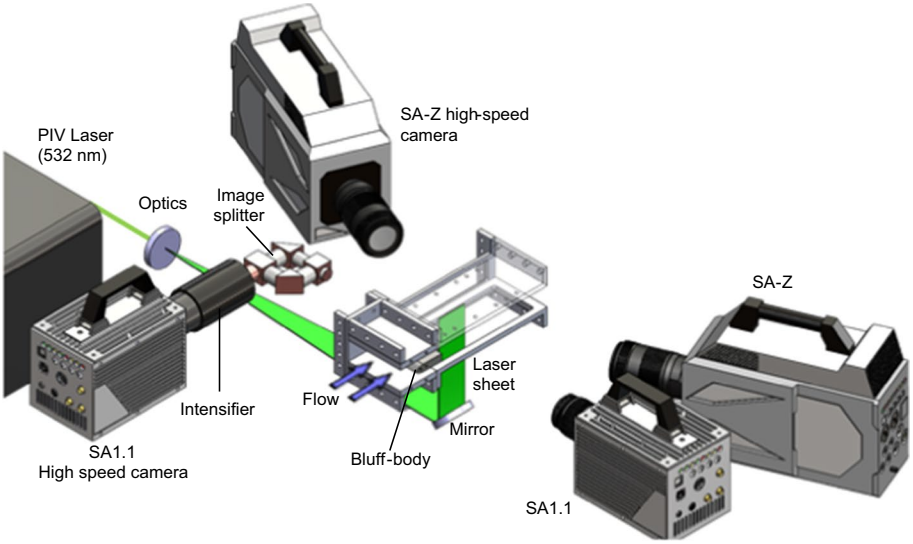

Fig. 4 High-speed optical diagnostics setup. One of the test section side walls has been removed for visual clarity

commercial software (LaVision DaVis 10) using a multi-pass cross-correlation algorithm and a 50% window overlap for interrogation regions. The final cross-correlation window size is 16×16 pixels (2×2 mm), which gives a velocity vector resolution of $\lambda_m \approx 1$ mm which is $\lambda_m/l_f \approx 2$ relative to the laminar flame thickness of a propane-air flame at $\Phi = 0.7$. The uncertainty in the velocity vectors is 0.25 m/s based on correlation statistics (Carr et al. 2009; Sciacchitano and Wieneke 2016).

Stereoscopic PIV images are collected using a pair of high-speed CMOS cameras (Photron SA-Z) mounted on opposite sides of the facility as depicted in Fig. 4. The cameras are oriented 22.5° from the wide-field cameras, and are equipped with 180 mm focal length, *f/4* macro objectives (Tamron), as well as scheimpflug adaptors to eliminate blurring from off-axis imaging. The cameras are focused on a smaller field of view of 24 × 24 mm between $1.8 \leq x/H \leq 3.4$ along the upper half of the domain as shown in Fig. 2a. Images are collected simultaneously with the wide-field PIV at 20 kHz. The image sensor is comprised of 1024×1024 pixels, giving a pixel resolution of 24 μm/pix. The stereo PIV images are also processed in LaVision DaVis software, with a final cross-correlation window size of 24×24 pixels (562×562 μm). The vector spacing for the stereo PIV data is $\lambda_m = 281$ μm, corresponding to $\lambda_m/l_f = 0.89$, and a velocity uncertainty of 0.05 m/s.

2.3.2 Chemiluminescence Imaging Systems

Along with the two PIV systems, a C_2*/CH* imaging system is employed to characterize the duration of the blowout process. The chemiluminescence from diatomic carbon (C_2*) and methylidyne (CH*) radical species are imaged on a high-speed CMOS camera (Photron SA1.1) with a 50 mm *f/1.2* lens. The camera and lens are coupled with a Lambert image intensifier (where the gain and gate values were kept constant amongst trials) and an image splitter, as shown in Fig. 4. The image splitter utilizes narrowband filters of 427 and 512 nm to isolate the C_2* and CH* species and collect two species images on

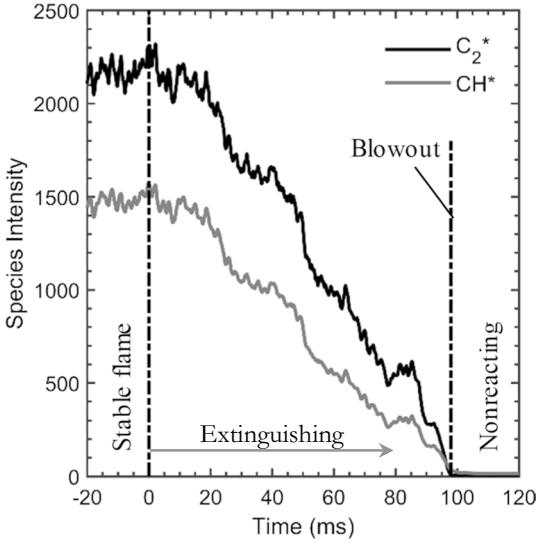

Fig. 5 An example of the mean C_2*/CH* species intensity during lean blowout

a single sensor. Specific details of the design, as well as a visualization of the split C_2*/CH* images, are provided by Reyes and Kailasanathan (2018). The field of view for the C_2*/CH* images match the wide-field PIV domain between $0.55 \leq x/H \leq 4.75$. Images are collected at 10 kHz, where each image aligns with every other PIV and SPIV image.

The intensity of the C_2* and CH* images are used to characterize the total duration of the blowout process. Throughout the extinction process, the chemiluminescence intensities of the C_2* and CH* will decrease until reaching a minimal constant value once the flame blows out. An example is provided in Fig. 5, where the mean intensity of the C_2* and CH* from a single blowout experiment is provided. The curves are obtained by calculating the average C_2* and CH* pixel intensity across the investigation domain, $2 \leq x/H \leq 4$. In Fig. 5, the time axis is aligned in a manner where $t = 0$ is the time instant where the extinction process begins, which is assessed as the instant where the flame luminosity begins to decrease from its initial stable value.

Imaging two radical species is advantageous, as the ratio of C_2*/CH* can be used to evaluate the instantaneous equivalence ratio (Morales et al. 2020a; Reyes and Kailasanathan 2018; Clark 1958; Jeong et al. 2006). In this study, the equivalence ratio is not a primary parameter of interest; however, temporal equivalence ratio curves were evaluated for each turbulence condition to verify the blowout equivalence ratio, which is presented in Table 1 and will be discussed later. Additional details of the methodology as well as the temporal curves can be found in a previous study (Morales et al. 2020b).

Additional experimental trials were executed to obtain independent CH* images, which were collected separately from the PIV and C_2*/CH* systems. The independent CH* system provides higher resolution images than the C_2*/CH* system, and is useful for quantifying global flame topography, heat release, and flame oscillations (Hardalupas and Orain 2004). The CH* system includes a high-speed CMOS camera (SA1.1) mounted perpendicular to the facility and a 427 nm optical filter. The domain of interest matches the wide-field PIV domain described above. Images are acquired at 20 kHz, onto a sensor comprised of 512 × 512 pixels, providing a pixel resolution of 131 µm/pix.

Table 1 Testing conditions and turbulence quantities for lean blowout experiments

Test case	Turbulence generator	u'_{rms} (m/s)	L_{11} (mm)	$Re = U_\infty H/\upsilon$	$\mathrm{Re}_{T = u'\mathrm{rms}L11/\upsilon}$	Φ_{BO}	t_{BO} (ms) $\pm \sigma$ (ms)
Low turb	N/A	0.9	15.1	25,700	871	0.52	113 ± 12
Mid turb	Static grid	2.8	8.1	25,700	1454	0.54	93 ± 14
High turb	Impinging jet grid	7.0	6.7A	25,700	3006	0.57	75.2 ± 19

2.4 Testing Conditions

The testing conditions for this study are detailed in Table 1. Three turbulence conditions are explored in this study: a low turbulence condition where there is no turbulence generator in the flow path, a mid turbulence condition where the turbulence generator is used as a static grid, and a high turbulence condition where the grid includes supersonic impinging jets. For all test conditions, the freestream velocity (U_∞) is kept constant at 25 m/s. The streamwise velocity fluctuations (u'_{rms}) and integral length scales (L_{11}) for each condition are provided in Table 1; both quantities are evaluated using the high-resolution SPIV data using the formulations provided in Eqs. (1) and (2) (Pope 2000). Specifically, both quantities are calculated within the freestream portions of the domain outside of the flame boundary, and an ensemble average is provided in Table 1. For all turbulence conditions explored here, the maximum Stokes number is $St = (\omega d_p/\nu)^{1/2} = 0.02$, the particle Reynolds number is $Re_p = 0.05$, and the stokes drag coefficient is $C_D = 24/Re_p = 480$ based on formulations provided in Ref. Melling (1997)

$$u'_{rms} = \left[\frac{1}{N-1} \sum_{i=1}^{N} \left(u - \bar{u} \right)^2 \right]^{1/2} \tag{1}$$

$$L_{11} = \int_{y_{min}}^{y_{max}} \frac{u'\left(x, y_0\right) * u'(x, y)}{u'\left(x, y_0\right)^2} dy \tag{2}$$

The turbulent velocity fluctuations and integral length scales are used to calculate the turbulent Reynolds number (Re_T) in Table 1. The blowout equivalence ratio (Φ_{BO}) is experimentally evaluated using the method from Ballal and Lefebvre (Ballal and Lefebvre 1979) and is also included in Table 1. The method involves slowly decreasing the fuel flow rate and documenting the flow rate when blowout occurs. The final column in Table 1 documents the total duration of the blowout process. The total duration (t_{BO}) is determined from chemiluminescence diagnostics (Kariuki et al. 2012), using the temporal species intensity curves to assess when the extinction process begins and when global blowout occurs; an example is provided in Fig. 5. The blowout durations in Table 1 represent an average value are calculated from an average of 10 experimental trails; the standard deviation (σ) amongst trials is also included.

3 Results and Discussion

The following sections present details regarding the fundamental behavior of the bluff-body flame for different turbulence conditions during a lean blowout transient. Details of the turbulence conditions explored for this study were discussed in Sect. 2.4 and relevant quantities were provided in Table 1. The first section of the results (Sect. 3.1) provides an overview of the flame structure and flow field during the lean blowout process and compares experimental observations with existing literature. Although much of the knowledge discussed in this section have already been discussed in previous literatures, it is beneficial to first visualize and describe the flame and flow behavior before delving into more detailed analysis. Once established, the true novelty of the results emerge; the subsequent sections (Sects. 3.2 and 3.3) explore the dominant flame and flow instabilities that occur during the blowout process and show that the instabilities are a function of turbulent flow properties. It is noted here that all instabilities discussed are purely a result of hydrodynamics, and no thermoacoustic instabilities were observed in experimentation or data. Once the hydrodynamic and turbulent flame-flow instabilities have been characterized, a theoretical description of the physical mechanism that induces the turbulent flame-flow oscillations is explored and validated in Sect. 3.4. The last section of the results (Sect. 3.5) then demonstrates that the flame-flow oscillations are linked with the flame strain rate, which is a critical parameter that initiates the local extinction process and drives a transition to global blowout.

3.1 Flame and Flow Visualizations

An overview of the lean blowout process for each turbulence condition is provided in Fig. 6. The timestamps on each contour are marked from the beginning of the blowout process, as exampled in Fig. 5. The contours in Fig. 6 depict the span-wise vorticity in the immediate bluff-body wake. This vorticity is induced from the flow separation that occurs at the trailing edge of the bluff-body, which is linked to the Kelvin–Helmholtz instability. The contours are overlaid with the instantaneous flame front, which is extracted from the wide-field PIV Mie scatter images. Specifically, the heat release from the flame induces a step-change in seed density in the PIV images, which has been used as a reliable marker for the location of the flame front over a range of Reynolds numbers (Tuttle et al. 2013; Pfadler et al. 2007). For this study, the flame front coordinates were extracted using an image processing technique described by Morales et al. (2020a); the technique involves enhancing the contrast between reactant and product regions through a series of median (Lim 1990) and complement filters, then binarizing the images using a statistically optimal threshold (Otsu 1979), and extracting flame front coordinates from the binarized images (Gonzalez et al. 2004). The instantaneous flame fronts in Fig. 6 are also superimposed with the local flame strain rate (κ), which is calculated using Eq. (3) (Roy Chowdhury and Cetegen 2017; Nair and Lieuwin 2007; Tuttle et al. 2013; Chung and Law 1984). It is noted that the flame front shown in Fig. 6 are not to scale, and have been enlarged to help visualize the local flame strain rate.

$$\kappa = -n_x n_y \left(\frac{\partial v}{\partial x} + \frac{\partial u}{\partial y} \right) + \left(1 - n_x^2\right) \frac{\partial u}{\partial x} + \left(1 - n_y^2\right) \frac{\partial v}{\partial y} \tag{3}$$

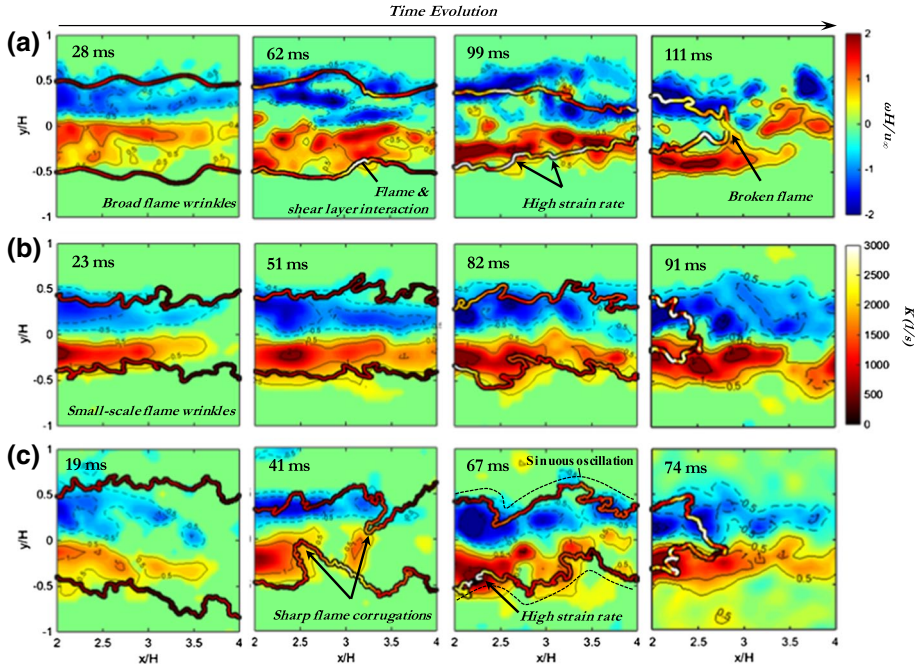

Fig. 6 Instantaneous flame front and vorticity fields during lean blowout for: **a** low turbulence, **b** mid turbulence, and **c** high turbulence cases. The local flame strain rate is superimposed onto the flame edge. To help visualize the local flame strain rate, the thickness of the flame fronts shown here have been artificially enlarged

For all turbulence conditions, the flame front characteristics change drastically during the lean blowout process. For the low turbulence condition, the flame is initially symmetric across the bluff-body centerline, and exhibits smooth, large-scale wrinkling. As the blowout process ensues, the flame loses its symmetric (varicose) character, and the wrinkles become smaller in scale. The changes to the flame topology are a result of a decreased flame speed and baroclinic torque in the reacting domain (Chaudhuri et al. 2010; Morales et al. 2019, 2020a; Tuttle et al. 2013; Geikie and Ahmed 2017). As the equivalence ratio is reduced, the flame speed will decrease and cause the flame to reside closer to the shear layer vorticity region. In tandem, the diminished baroclinic torque production along the flame front will allow the shear layer vorticity to increase in magnitude. Combined, these effects lead to flame and shear layer interactions (Shanbhogue et al. 2009; Tuttle et al. 2013; Chowdhury and Cetegen 2018), as depicted in the low turbulence case in Fig. 6 (62 ms). As the equivalence ratio is decreased further, the flame experiences a notable necking feature (at 99 ms) and finally begins to extinguish between $3 \leq x/H \leq 4$ (111 ms).

Between the three test cases, there are notable differences in flame topology at elevated turbulence conditions. At high turbulence conditions, the flame front experiences more drastic topological features such as sharp flame corrugations (41 ms) and an early onset of a sinuous oscillation (67 ms) (Shanbhogue et al. 2009; Emerson and O'connor 2012). The sinuous oscillations are associated with a transition to an absolute instability mode where the flame and flow field resemble the Bénard von-Kármán (BVK) instability. This transition to the BVK instability mode is critical, and has been previously associated with the "second stage" of the

blowout process (Shanbhogue et al. 2009; Nair and Lieuwin 2007), in which the flame has surpassed the point of localized extinctions and is in the final stage prior to global blowout. The early onset of the absolute instability for the high turbulence case suggest that the transition to non-reacting flow conditions is accelerated with turbulence, and global blowout is expedited. This conclusion is also supported by the average blowout duration and increased blowout equivalence ratios provided in Table 1.

3.2 Flame Instabilities: POD and DMD Analysis

The flame structure is analyzed for each turbulence condition to identify if there are distinct characteristics, oscillations, or coherent structures. For this study, spectral analysis was initially conducted using Fourier transform and Welch methods (Welch 1967); however, the flame and flow spectra tend to lose narrowband peaks at highly turbulent conditions and the spectra resembles a broadband Kolmogorov decay. For this reason, dimensional reduction techniques of proper orthogonal decomposition (POD) and dynamic mode decomposition (DMD) are applied to quantify turbulent flame oscillation modes. The approach is similar to the method described by Higham et al. (2018), in which POD is first applied to the flame images to home in on the dominant coherent flame oscillations. Once identified, these spectral peaks are targeted in dynamic mode decomposition (DMD) to characterize the physical structure associated with the flames oscillating modes. For each turbulence condition, POD and DMD analysis was performed among multiple trials to ensure results were consistent.

Proper orthogonal decomposition (POD) is a technique that identifies spatially correlated modes from a set of observations (or snapshots). POD is advantageous as it's a purely data-driven technique and has been previously implemented to study flame instabilities for various configurations, including bluff-body flames (Blanchard et al. 2014; Kostka et al. 2012). The general method of extracting POD modes is outlined in Eq. (4) (Kutz et al. 2016). Instantaneous snapshots of data (x) are first compiled into column vectors $\vec{x}^{(i)}$ as in Eq. (4a). The instantaneous vectored data is then compiled into an $M \times N$ matrix X in Eq. (4b), where M represents the number of datapoints per snapshot, and N represents the number of snapshots; in this case, the snapshots are images with a resolution of 512 ×× 512 pixels ($M = 262{,}144$), and N is the number of images in the blowout data ($N \sim 1500$–2300). The average value of the reshaped data matrix is subtracted from itself, and a singular value decomposition (SVD) is performed on the matrix. The output of the SVD provides three separate matrices: U, Σ, and V^* in Eq. (4c). The U matrix contains the eigenvectors of the data matrix, which represent the POD modes. V represents the temporal evolution of each mode, and Σ is a diagonal matrix of singular values that determines the rank of the POD modes. Each of these matrices are arranged hierarchically based on each modes energy in the dataset.

$$\vec{x}^{(i)} = \begin{bmatrix} x_1^{(i)} \\ x_2^{(i)} \\ x_3^{(i)} \\ \vdots \\ x_M^{(i)} \end{bmatrix} \tag{4a}$$

$$X = \begin{bmatrix} \vec{x}^{(1)} & \vec{x}^{(2)} & \vec{x}^{(3)} & \dots & \vec{x}^{(N)} \end{bmatrix} \tag{4b}$$

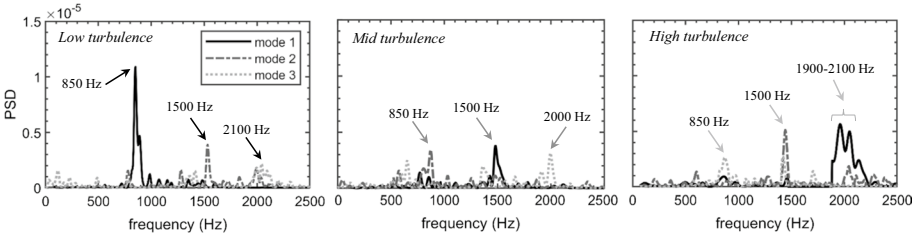

Fig. 7 POD spectra showing the first 3 coherent modes for different turbulence conditions

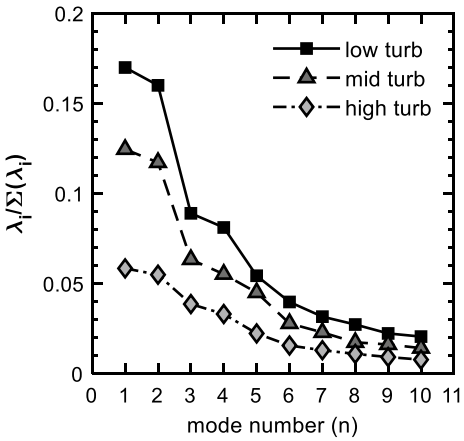

Fig. 8 Modal energy content from POD analysis

$$X = U\Sigma V * \tag{4c}$$

For this analysis, the POD is applied to the CH* images to provide a globalized perspective of the flame and heat release oscillations during lean blowout. For all POD analysis, the most energetic mode (noted here as mode 0) typically represents time averaged flow features. For this study, mode 0 is not presented or discussed since it does not provide any significant insight into the temporal flame dynamics. The POD results for each turbulence condition are provided in Fig. 7. Here, three modes are presented; mode 1 represents most energetic mode that is captured in the flame images, and the subsequent modes (2 and 3) each have a diminished energy contribution with respect to the previous mode. For reference, the energy content of the first 10 modes is provided in Fig. 8. For the low turbulence condition, the POD spectra has a dominant peaks at 850, 1500, and 2100 Hz, where the 850 Hz oscillation is the most energetic and largest in amplitude. Interestingly, the same three frequency peaks are noticed for the mid and high turbulence conditions; however, the highest amplitude mode (mode 1) shifts to higher frequencies as the turbulence intensity increases. For the mid turbulence case, the most energetic mode is the 1500 Hz mode, while the high turbulence case favors the ~ 2100 Hz mode. It is also noted that the high-frequency oscillations in for the high turbulence case have a broader distribution than the low and mid turbulence cases. This is not surprising, as the turbulent energy cascade tends to distribute spectral energy amongst a range of frequencies.

DMD is also applied to the CH* images. DMD is a technique that extracts coherent spatial modes from time-resolved data. The advantage of DMD is that is specifically targets dynamics and provides a spectra for dynamic instabilities. Specifically, DMD can assess the temporal evolution of spatially correlated POD modes, thus providing a frequency spectra of time-resolved data along with temporal growth or decay rates of the modes (Kutz et al. 2016).

The governing equation for DMD is given in Eq. (5) (Kutz et al. 2016). $X^{\dagger}$ is the pseudoinverse of the reshaped data matrix (X), X' is the same data matrix but shifted one step forward in time, and A is the linear operator that advances X to X'. Each DMD mode is an eigenvector of A, and the DMD modes each correspond to a specific eigenvalue of A. The linear operator A is found by first taking an SVD of the reshaped data matrix, X. To optimize computational efficiency, an SVD reduction is used to truncate low-rank data. Low dimensional structures in the data are truncated based on the singular values, Σ from Eq. (4c), which decreases to zero after a limited number of dominant modes. Truncating these low-ranked structures vastly improves computational costs while having a negligible effect on the accuracy of the results. $\tilde{A}$, the reduced dynamic linear operator based on the SVD reduction, is calculated by using the pseudoinverse of X from the SVD as in Eq. (5b). Note, the SVD is described in Eq. (4c), and U in Eq. (5b) represent the POD modes. The eigendecomposition of $\tilde{A}$ yields W and Λ, the eigenvectors and eigenvalues of $\tilde{A}$ respectively, Eq. (5c). A reconstruction of the eigendecomposition gives the DMD modes (φ), Eq. (5d).

$$A = X'X^{*} \tag{5a}$$

$$\tilde{A} = U^{*}X'V\Sigma^{-1} \tag{5b}$$

$$\tilde{A}W = W\Lambda \tag{5c}$$

$$\varphi = X'V\Sigma^{-1}W \tag{5d}$$

The physical structures associated with the oscillating flame modes are visualized by the DMD results in Fig. 9. The contours are a visual representation of temporal flame oscillations, and although they are extracted from the sequence of CH* images, they do not represent an average quantity. To help interpret the physical structures of the DMD contours, instantaneous CH* flame fronts are overlaid onto the mid turbulence case to help visualize the flame topology associated with the specific modes. In Fig. 9, the flame structure tends to wrap around the DMD contours, which suggests that the dominant frequencies are linked with the flame wrinkles. This is somewhat expected, since the DMD algorithm is applied to the time sequence of CH* images, and chemiluminescence is a marker for heat release, it makes sense that the flame structure matches well with the DMD contours. Furthermore, the true advantage of using these decomposition techniques is that the physical structures associated with the oscillation modes can be identified. For instance, using the DMD contours and flame structures in Fig. 9, a length-scale λ is defined; here, λ is based on the physical structures seen in the DMD contour, which closely matches half of the flames wrinkle wavelength. This is highly advantageous, and provides an avenue to compare the flame structures with the oscillation modes identified in Fig. 9.

The most energetic flame oscillation frequency (f_{POD}) and corresponding length scale λ, are plotted in Fig. 10. For each turbulence case, the λ value was evaluated as the average axial length of the DMD contours (as shown in Fig. 9). In Fig. 10, the flame oscillation

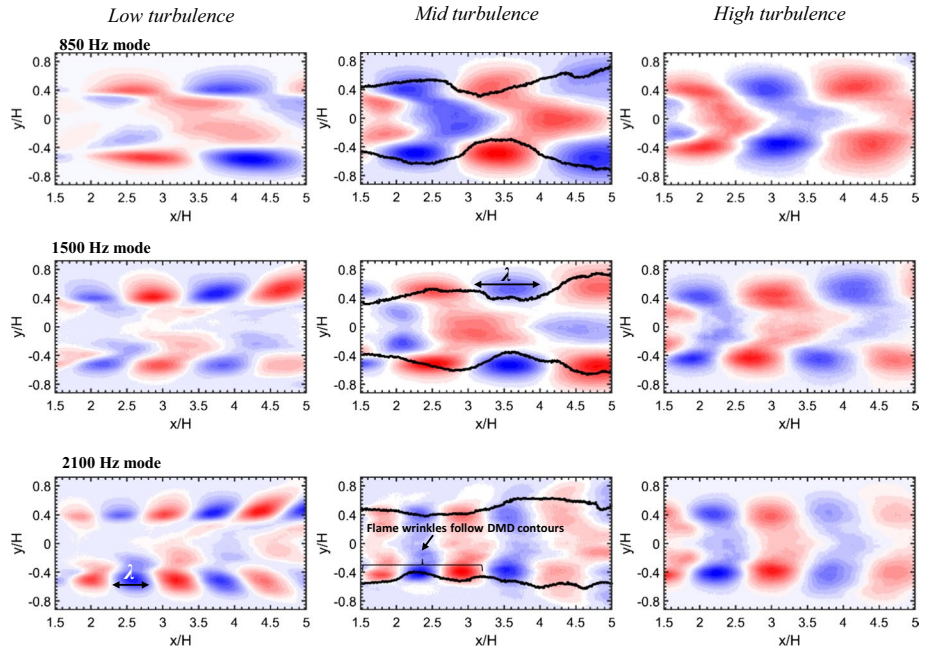

Fig. 9 DMD contours depicting the dominant oscillatory flame modes

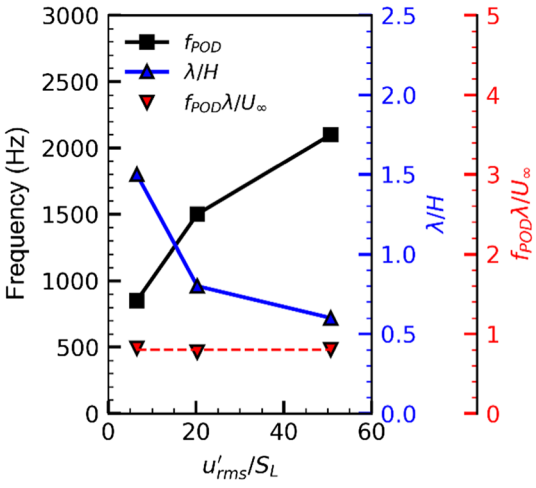

Fig. 10 Dominant flame oscillation frequency, wrinkling scale (λ), and nondimensional number $f_{POD}\lambda/U_\infty$

frequency and wrinkling scale appear to have an inverse relationship. Under further investigation, it is determined that the product of the two quantities provide a nominally constant value. Thus, the oscillation frequency of the flame (f_{POD}), wrinkle-scale (λ), and freestream velocity (U_∞) are used to define a non-dimensional number, $f_{POD}\lambda/U_\infty$, and included in Fig. 10. Using this formulation, the frequency data collapses to a nondimensional value of 0.8. This confirms that there is a strong relationship between the flame oscillations

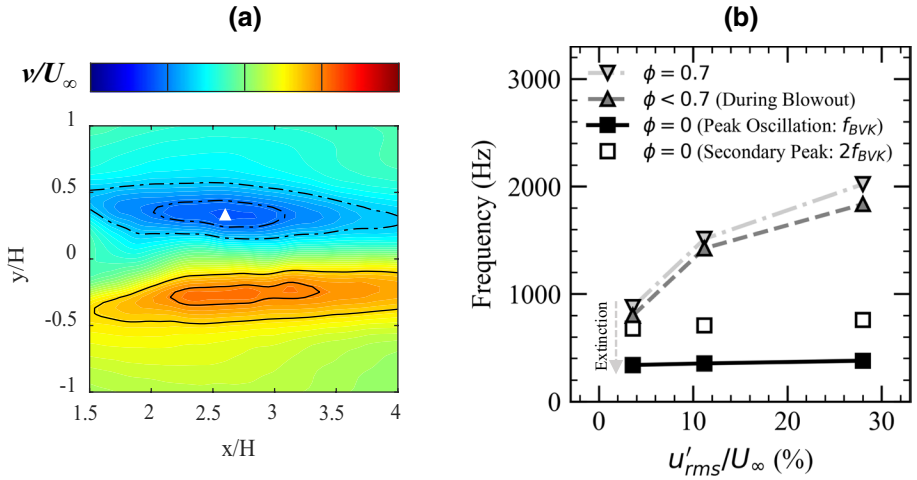

Fig. 11 **a** An example of the time-averaged transverse velocity (v) field taken from the low turbulence condition. The white triangle near the center represents the location of the largest v-velocity magnitude where the flow frequency analysis is conducted. **b** The peak flow field oscillation frequency (f_{flow}) as a function of equivalence ratio (Φ)

and flame wrinkling scale. However, bluff-body flame wrinkles are driven from the convecting instabilities in the shear layers. For this reason, it is beneficial to investigate the hydrodynamic instabilities within the domain to discern the source of the flame wrinkling characteristics.

3.3 Hydrodynamic Instabilities

A spectral analysis of the flow field is conducted for each turbulence condition using the PIV data. The flow spectra is assessed using the transverse velocity signal (v), which mitigates contributions from the stream-wise bulk flow (Morales et al. 2019). For each case, a time-averaged velocity field is used to determine the spatial location where the transverse velocity is a maximum. An example of a time-averaged transverse velocity field is provided in Fig. 11a, and the spatial location of maximum velocity is marked. The temporal v-velocity signal at this location is used for spectral analysis, which is conducted using Welch's method (Welch 1967). The spectral peaks obtained from the analysis are provided in Fig. 11b. A stable condition of $\Phi = 0.7$ and a non-reacting case of $\Phi = 0$ are also included to visualize the combined effects of the equivalence ratio and turbulence on flow field oscillations. Since the laminar flame speed will change with the equivalence ratio, the x-axis in Fig. 11 is presented as u'_{rms}/U_{∞}, rather than u'_{rms}/S_L. For all turbulence conditions, the peak oscillation frequency observed during blowout is slightly less than the stable condition of $\Phi = 0.7$. This trend is expected, and has been discussed in literatures (Morales et al. 2019; Emerson and O'connor, J., Juniper, M., Lieuwen, T. 2012). The decrease in flow oscillation frequency will occur until the flame blows out, and the bluff-body wake locks into the asymmetric Bénard von-Karman (BVK) instability when $\Phi = 0$. Figure 11 also reveals that there is a drastic increase in the flow oscillation frequency as the turbulence intensity is increased. The spectral peaks during blowout closely match the flame

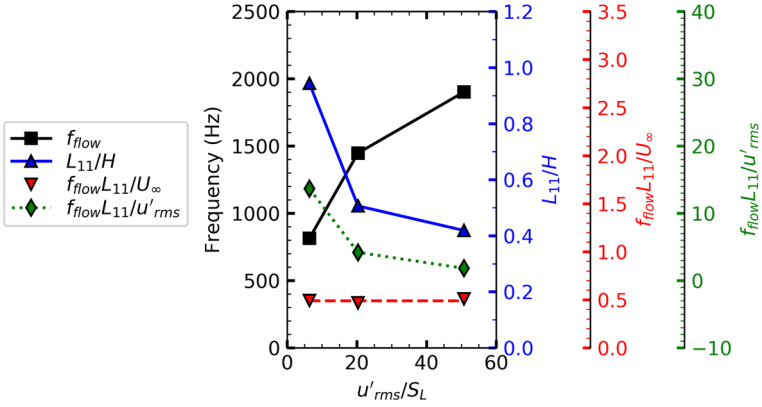

Fig. 12 Flow oscillation frequency, integral length scales, and nondimensional numbers $f_{flow}L_{11}/U_\infty$ and $f_{flow}L_{11}/u'_{rms}$. f_{flow} is calculated from the spectral analysis of the flow field, previously shown in Fig. 11. $f_{flow}L_{11}/U_\infty$ collapses the data to a unified value, unlike $f_{flow}L_{11}/u'_{rms}$

oscillations determined from POD and DMD analysis, which confirms that the flame and flow oscillations are coupled.

Previous literatures (Morales et al. 2019, 2020a) have shown that the dominant flame-flow oscillations prior to lean blowout closely match the first harmonic of the BVK instability ($2f_{BVK}$). For reference, the first BVK harmonic frequency is also depicted in Fig. 11b. For the low turbulence condition, it is noticed that this trend is upheld, and the flow field oscillations closely match the first BVK harmonic ($2f_{BVK} \approx$ 850–900 Hz). However, this does not hold true for the mid and high turbulence conditions, which lock into frequencies near 1500 and 1900 Hz, respectively. The high frequency oscillations for the mid and high turbulence cases are expected to be a direct result of the turbulent flow. However, the link between the turbulent flow properties and the flame-flow frequencies in Fig. 11 are not yet clear. It is noted, however, that the flow oscillation frequencies in Fig. 11 closely match the dominant POD modes previously shown in Fig. 7. However, Fig. 7 also revealed that the 850 Hz mode did not completely disappear with elevated turbulence, but was suppressed in favor of the higher frequency modes. Since the behavior of flames and turbulent flows are tightly coupled (Lipatnikov et al. 2014; Dopazo et al. 2017; Chakraborty et al. 2016), it is expected that a similar phenomenon occurs for the flow field. In other words, the first harmonic mode does not completely disappear, but is suppressed if favor of high frequency oscillations, which are expected to be a direct result of the turbulent flow.

The remaining question that we seek to address is: how exactly does turbulence induce the specific frequencies seen in Fig. 11? One approach to answer this question is to determine if a relevant flow-driven length scale can collapse the frequency data to a unified value, thereby isolating a key variable. Among many relevant fluid and turbulent length scales, the integral length scales and freestream velocity were determined to best collapse the frequency data to a unified value. The results are shown in Fig. 12, which depicts the flow frequency (f_{flow}), the integral length scale (L_{11}), and a nondimensional number $f_{flow}L_{11}/U_\infty$. Using the integral length scale, the flame-flow frequencies collapse to a unified value of 0.49. This is an interesting result, since one may have expected that the turbulent velocity scales (u'_{rms}) would be a more viable choice for the velocity scale in the nondimensionalization. However, the tabulated values of $f_{flow}L_{11}/u'_{rms}$ do not collapse to a unified value

Table 2 Eddy convecting timescale and frequency for different turbulence conditions

Turbulence Condition	L_{11} (mm)	τ_{conv} (μs)	f_{conv} (Hz)
Low	15.1	604	1656
Mid	8.1	324	3086
High	6.7	268	3731

and are 13.7, 4.2, and 1.8 for the low, mid, and high turbulence cases respectively. This occurs because the product of $f_{flow}L_{11}$ is nominally constant between the three cases tested here. Therefore, when divided by a constant freestream velocity U_{∞}, a nominally constant nondimensional number can be obtained.

3.4 Mechanistic Description of the Turbulent Flame Oscillations

The unified value of $f_{flow}L_{11}/U_{\infty}$ above suggests that the high frequency oscillations for the mid and high turbulence cases are driven from the integral scale eddies in the flow. This conclusion is also supported by previous literatures (Steinberg and Dirscoll 2009; Driscoll et al. 2020; Damkohler 1937), which describe how turbulent eddies influence the topology and wrinkling characteristics of the flame front. Essentially, turbulent eddies will promote small-scale wrinkling along the flame front and induce high frequency transverse flame oscillations seen in Figs. 7 and 9. Although this knowledge is beneficial, it still does not address how the integral scale eddies induce the specific oscillation frequencies seen in Figs. 7 and 9. The subsequent analysis seeks to answer this question.

For the low turbulence conditions in this study, there is no turbulence generator installed into the flow path, and the flame naturally oscillates at 850 Hz due to the bluff-body shear layer instabilities (Emerson and O'connor 2012). However, the addition of the turbulence generator will inject turbulent energy into the flow; in particular, the turbulent kinetic energy will be greatest for the integral scale eddies. These eddies will convect in a freestream with mean velocity U_{∞}. The timescale in which these eddies are convected into the flame front can be defined using a timescale, $\tau_{conv}=L_{11}/U_{\infty}$. The inverse of this timescale provides a frequency, f_{conv}, which represents the frequency that integral scale eddies are propagated into the flame. The eddy convecting timescale and corresponding frequency for each turbulence condition is provided in Table 2.

It is proposed that f_{conv} will have a superimposing effect on the natural flame-flow oscillations. For instance, experimental literatures have previously depicted the effect of *a singular* large-scale eddy on the structure and topology of a premixed flame (Steinberg and Dirscoll 2009; Skiba et al. 2019). The eddy will both increase the thickness of the flame, but will also induce new flame wrinkles on the order of the eddy length scales. In this manner, the eddy has a perturbing effect on the structure of the flame and induces a small-scale flame oscillation. However, in a practical archetypical combustor, a flame will be continuously subjected to turbulent perturbations and eddies. For the current experiment, the timescale in which the eddy-induced flame oscillation will repeat itself is expected to be $\sim\tau_{conv}$ (or inversely f_{conv}). Thus, as eddies are propagated at the flame at a frequency of f_{conv}, it is anticipated that this will induce an oscillation that will superimpose onto the natural oscillations that would occur for a non-turbulent flame. This effect is illustrated in Fig. 13a, where 3 oscillation signals are shown. The first signal is a sine wave oscillating at 850 Hz;

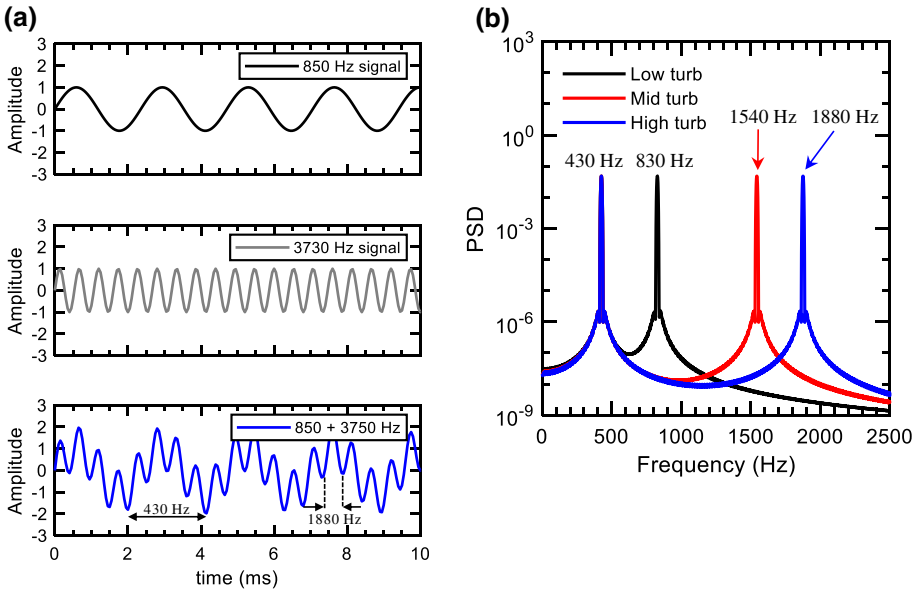

Fig. 13 **a** Sine waves representing the natural flame oscillation, eddy convection frequency for the high turbulence condition, and the sum of each signal. **b** Frequency spectra from superimposed flame and eddy convection frequencies for each turbulence case

this represents the natural flame oscillation induced from the shear layers with no effects of induced turbulence. The second signal is a sine wave oscillating at 3730 Hz, which represents the frequency that the turbulent eddies are convected into the flame for the high turbulence case. If the two signals are added, a third signal is obtained; this third signal represents the superimposed effect the integral-scale eddies would have on the flame-flow oscillations.

A spectral analysis is performed on the superimposed signal from Fig. 13a and the resulting frequency spectra is provided in Fig. 13b. The same process is repeated for the low and mid turbulence cases, and the resulting spectra (obtained from the addition of the natural flame oscillation of 850 Hz and the corresponding eddy convection frequency) are also included in Fig. 13b. For all conditions, the peak frequencies very closely match the flame-flow oscillations found from POD and flow analysis. Thus, it appears that flame-flow oscillations are indeed driven from the superposition of turbulent eddies onto the unforced reacting flow oscillations.

3.5 Flame Strain Rate

The analysis from the previous sections indicate that integral scale eddies influence the hydrodynamic instabilities in the bluff-body wake, which subsequently alters the flame-flow oscillation frequencies during the lean blowout process. However, hydrodynamic instabilities and flame-flow oscillations will also influence the flame strain rate (Morales et al. 2019; An and Steinberg 2019), which is an important parameter that drives local extinction and global blowout. As such, this section describes the effects of turbulence on

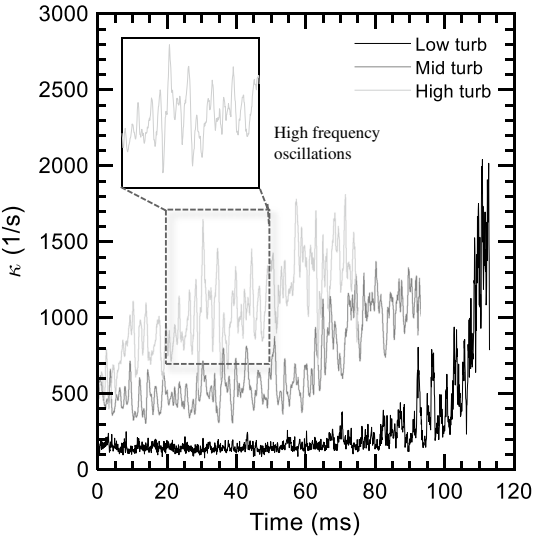

Fig. 14 Flame strain rate during lean blowout for all turbulence conditions

the flame strain rate, and provides additional details of how the turbulence-driven flame-flow oscillations influence the lean blowout process.

The local flame strain rate is first calculated along the flame front using Eq. (3), and visual examples are depicted in Fig. 6. The flame strain rate is then spatially averaged within the domain ($2 \leq x/H \leq 4$) to provide a statistical representation of the flame strain rate evolution during blowout. The strain rate curves for each turbulence condition are provided in Fig. 14. The curves are intentionally selected from a single set of data rather than an average of multiple experimental trials, since averaging would naturally filter out the temporal oscillations which are of key interest for this study. All curves are temporally aligned so that they all begin at $t = 0$, which is defined as the time instant where the extinction process begins (see Fig. 5). It is first noticed that the magnitude of the flame strain rate increases with turbulence. The increased strain rate magnitude is driven from the turbulent eddies in the freestream portions of the domain. The velocity fluctuations induced from turbulent eddies will cause increased hydrodynamic strain rates in the freestream, which in turn drives high strain rate magnitudes along the flame. The increased magnitude of the flame strain rate will expedite the local extinction process and accelerate the global blowout process. Additionally, the temporal evolution for each turbulence condition is visually different. For instance, the low turbulent flame maintains a nominally low strain rate throughout most of the blowout duration. Only during the last $\approx$ 30 ms of its lifetime does the flame strain rate increase at an exponential rate. In contrast, the highly turbulent flame appears to grow in a linear fashion during its lifetime. Thus, the temporal dynamics of the blowout process are heavily influenced by turbulence. This is also consistent with Fig. 6, where the highly turbulent flame experienced an early onset of sinuous oscillations.

For all conditions, the flame strain rate exhibits a highly oscillatory behavior during the lean blowout process. Visually, it appears the amplitude of these oscillations also increases with turbulence. To quantify the flame strain rate oscillations, a frequency analysis is performed on the curves in Fig. 14. However, in order to isolate the flame strain rate oscillations without any effects of the temporally increasing values, the strain signals in Fig. 14 are subtracted from a sliding window to create "new" strain rate curves that oscillate about

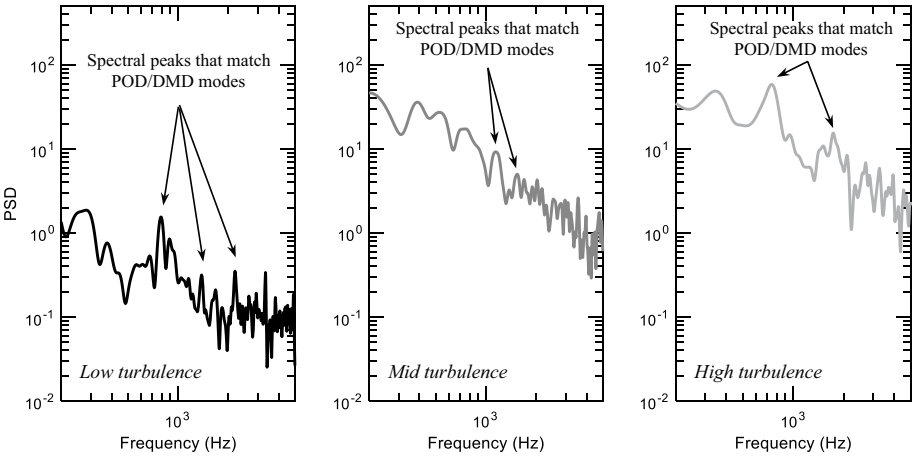

Fig. 15 Spectra of the temporal strain rate during lean blowout

a zero mean. The window size used here was 2.5 ms, which is ~ 3% of the total blowout duration. The frequency analysis is conducted on the "new" strain rate curves, and the corresponding spectra are shown in Fig. 15. There are distinct differences in the strain rate spectra for each turbulence condition. The low turbulence case has multiple narrowband peaks, while the high turbulence case has a range of frequencies coalescing into broad spectral peaks. For each turbulence case, there are spectral peaks that match the frequency modes from POD and flow-field analysis, as marked on the figure. Thus, the flame strain rate oscillations and magnitude are a strong function of turbulence. A higher oscillation frequency will increase the probability that the instantaneous strain rate will exceed the extinction strain rate limit. Thus, local extinction can occur more frequently for highly turbulent flames. This, combined with the increased strain rate magnitude shown in Fig. 14, accelerates the global blowout process and causes the flame to blowout at higher equivalence ratios (Table 1). Since the flame, flow, and strain rate oscillations are driven from turbulent length scales (L_{11}) and the strain magnitudes are elevated with turbulent velocity scales (u'_{rms}), the extinction and blowout process becomes more probable in the presence of small-scale,[1] high intensity turbulence.

4 Conclusions

Flame, flow, and strain rate instabilities were investigated during lean blowout of premixed bluff-body flames. The flame structure became more corrugated with elevated turbulence intensities, and smaller-scale wrinkling structures were observed. Upon further

[1] Based on the analysis, the oscillation frequency should increase as the integral length scale decreases. To be more precise, this is only true if the integral length scales are larger than the laminar flame thickness ($L_{11} > l_f$). Based on Damköhler's hypothesis (Damkohler 1937), turbulent eddies that are smaller than the flame thickness will primarily influence thermal and diffusive transport in the flame, whereas eddies larger than the flame thickness will primarily distort the flame front, and thus alter the dominant oscillations and extinction process.

investigation, POD and DMD analysis revealed that the smaller-scale wrinkling structures were linked with higher transverse flame oscillation frequencies at elevated turbulence conditions. The DMD results were used to define a characteristic wrinkling scale λ, which represents half of a full wrinkle wavelength. Using this wrinkle scale, a unified non-dimensional number was defined as $f_{POD}\lambda/U_\infty$, which collapsed the frequency data to a unified nondimensional value.

To assess the source of the increased oscillation frequency, the flow-field instabilities were investigated. The flow field exhibited spectral peaks that matched the flame oscillations from POD analysis; thus, the flame oscillations were attributed to hydrodynamics. Specifically, the flame and flow oscillations were linked to the integral length scales. It was determined that fL_{11}/U_∞ collapsed to a unified nondimensional number for all turbulence conditions. Additionally, the specific flame-flow frequencies were attributed to a superimposed effect where integral scale eddies interact with the flame front at a frequency $f_{conv} = 1/\tau_{conv} = U_\infty/L_{11}$. The interaction of the integral scale eddies, combined with the natural flame oscillations that occur without induced turbulence, invoke high frequency flame-flow oscillations during lean blowout.

During the blowout process, the flame strain rate oscillations matched the flame-flow oscillations. Flame strain rate oscillations favored higher frequencies at elevated turbulence conditions. Additionally, increasing the turbulent velocity fluctuations increased the magnitude of the flame strain rate. Combined, this increases the likelihood for local extinctions to occur along the flame front, and supports that turbulence will accelerate the lean blowout process. Thus, the likelihood of extinction and blowout becomes more probable at highly turbulent conditions with large velocity fluctuations (u'_{rms}) and small length scales (L_{11}) that approach the order of the flame thickness.

Acknowledgements This material is based upon work supported by the Air Force Office of Scientific Research. The authors would also like to acknowledge Dr. Campbell Carter at the AFRL for providing equipment support for performing these experiments.

Funding This study was funded by the Air Force Office of Scientific Research award numbers 16RT0673/FA9550-16–1-0441 and 19RT0258/FA9550-19–0322 by Program Manager: Dr. Chiping Li.

Declarations

Conflict of interest All authors have declare that they have no conflict of interest.

References

An, Q., Steinberg, A.M.: The role of strain rate, local extinction, and hydrodynamic instability on transition between attached and lifted swirl flames. Combust. Flame. **199**, 267–278 (2019)

Ballal, D., Lefebvre, A.H.: Weak extinction limits of turbulent flowing mixtures. J. Eng. Power. **101**, 343–348 (1979)

Blanchard, R., Wickersham, A.J., Ma, L., Ng, W., Vandsburger, U.: Simulating bluff-body flameholders: on the use of proper orthogonal decomposition for combustion dynamics validation. J. Eng. Gas Turbines Power. **136**, 1–10 (2014)

Candel, S.: Combustion dynamics and control: progress and challenges. Proc. Combust. Inst. **29**, 1–28 (2002)

Carr, Z., Ahmed, K., Forliti, D.: Spatially correlated precision error in digital particle image velocimetry measurements of turbulent flows. Exp. Fluids. **47**, 95–106 (2009)

Chakraborty, N., Konstantinou, I., Lipatnikov, A.: Effects of Lewis number on vorticity and enstrophy transport in turbulent premixed flames. Phys. Fluids. **28**, 10 (2016)

Chaudhuri, S., Kostka, S., Renfro, M.W., Cetegen, B.M.: Blowoff dynamics of bluff body stabilized turbulent premixed flames. Combust. Flame. **157**, 790–802 (2010)
Chaudhuri, S., Kostka, S., Tuttle, S.G., Renfro, M.W., Cetegen, B.M.: Blowoff mechanism of two dimensional bluff-body stabilized turbulent premixed flames in a prototypical combustor. Combust. Flame. **158**, 1358–1371 (2011)
Chowdhury, B.R., Cetegen, B.M.: Effects of free stream flow turbulence on blowoff characteristics of bluff-body stabilized premixed flames. Combust. Flame. **190**, 302–316 (2018)
Chung, S.H., Law, C.K.: An invariant derivation of flame stretch. Combust. Flame. **55**, 123–125 (1984)
Clark, T.P.: Studies of OH, CH, and C2 radiation from laminar and turbulent propane-air and ethylene-air flames-NACA technical note References 4266, p. 23 (1958)
Damkohler, G.: Influence of diffusion, fluid flow, and heat transport on the yield in chemical reactors. Der Chem. Ign. **3**, 359–485 (1937)
Dopazo, C., Cifuentes, L., Chakraborty, N.: Vorticity budgets in premixed combusting turbulent flows at different Lewis numbers. Phys. Fluids. **29**, 1–14 (2017)
Driscoll, J.F., Chen, J.H., Skiba, A.W., Carter, C.D., Hawkes, E.R., Wang, H.: Premixed flames subjected to extreme turbulence: some questions and recent answers. Prog. Energy Combust. Sci. **76**, 51 (2020)
Emerson, B., Oconnor, J., Juniper, M., Lieuwen, T.: Density ratio effects on reacting bluff-body flow field characteristics. J. Fluid Mech. **706**, 219–250 (2012)
Erickson, R.R., Soteriou, M.C.: The influence of reactant temperature on the dynamics of bluff body stabilized premixed flames. Combust. Flame. **158**, 2441–2457 (2011)
Geikie, M.K., Ahmed, K.A.: Lagrangian mechanisms of flame extinction for lean turbulent premixed flames. Fuel **194**, 239–256 (2017)
Geikie, M.K., Carr, Z.R., Ahmed, K.A., Forliti, D.J.: On the flame-generated vorticity dynamics of bluff-body-stabilized premixed flames. Flow Turbul. Combust. **99**, 487–509 (2017)
Gonzalez, R.C., Woods, R.E., Eddins, S.L.: Digital Image Processing Using MATLAB. Pearson Prentice Hall, New Jersey (2004)
Hardalupas, Y., Orain, M.: Local measurements of the time-dependent heat release rate and equivalence ratio using chemiluminescent emission from a flame. Combust. Flame. **139**, 188–207 (2004)
Herbert, M.V.: Aerodynamic influences on flame stability. Prog. Combust. Sci. Technol. **5**, 61–109 (1960)
Higham, J.E., Brevis, W., Keylock, C.J.: Implications of the selection of a particular modal decomposition technique for the analysis of shallow flows. J. Hydraul. Res. **56**, 796–805 (2018)
Jeong, Y.K., Jeon, C.H., Chang, Y.J.: Evaluation of the equivalence ratio of the reacting mixture using intensity ratio of chemiluminescence in laminar particlly premixed CH4-air flames. Exp. Therm. Fluid Sci. **30**, 663–673 (2006)
Kariuki, J., Dawson, J.R., Mastorakos, E.: Measurements in turbulent premixed bluff body flames close to blow-off. Combust. Flame. **159**, 2589–2607 (2012)
Kostka, S., Lynch, A.C., Huelskamp, B.C., Kiel, B.V., Gord, J.R., Roy, S.: Characterization of flame-shedding behavior behind a bluff-body using proper orthogonal decomposition. Combust. Flame. **159**, 2872–2882 (2012)
Kutz, J.N., Brunton, S.L., Brunton, B.W., Proctor, J.L.: Dynamic Mode Decomposition: Data-Driven Modeling of Complex Systems. Society for Industrial and Applied Mathematics, Philadelphia (2016)
Lignell, D.O., Chen, J.H., Schmutz, H.A.: Effects of Damköhler number on flame extinction and reignition in turbulent non-premixed flames using DNS. Combust. Flame. **158**, 949–963 (2011)
Lim, J.S.: Two-Dimensional Signal and Image Processing. Prentice Hall, Englewood Cliffs (1990)
Lipatnikov, A.N., Nishiki, S., Hasegawa, T.: A direct numerical simulation study of vorticity transformation in weakly turbulent premixed flames. Phys. Fluids. **26**, 1–16 (2014)
Longwell, J.P., Frost, E.E., Weiss, M.A.: Flame Stability in Bluff Body Recirculation Zones. Ind. Eng. Chem. **1**(45), 1629–1633 (1953a)
Longwell, J.P., Frost, E.E., Weiss, M.A.: Flame stabilization by bluff bodies and turbulent flames in ducts. Proc. Combust. Inst. **4**, 90–97 (1953b)
Lovett, J.A., Brogan, T.P., Philippona, D.S., Keil, B. V., Thompson, T.V.: Development Needs for Advanced Afterburner Design. AIAA/ASME/SAE/ASEE Joint Propulsion Conference and Exhibit (2004)
Markovich, D.M., Abdurakipov, S.S., Chikishev, L.M., Dulin, V.M., Hanjalić, K.: Comparative analysis of low- and high-swirl confined flames and jets by proper orthogonal and dynamic mode decompositions. Phys. Fluids. **26**, 10 (2014)
Masri, A.R., Bilger, R.W., Dibble, R.W.: The local structure of turbulent nonpremixed flames near extinction. Combust. Flame. **81**, 260–276 (1990)
Melling, A.: Tracer particles and seeding for particle image velocimetry. Meas. Sci. Technol. **8**, 1406–1416 (1997)

Morales, A.J., Lasky, I.M., Geikie, M.K., Engelmann, C.A., Ahmed, K.A.: Mechanisms of flame extinction and lean blowout of bluff body stabilized flames. Combust. Flame. **203**, 31–45 (2019)
Morales, A.J., Reyes, J., Joo, P.H., Boxx, I., Ahmed, K.A.: Pressure gradient tailoring effects on the mechanisms of bluff-body flame extinction. Combust. Flame. **215**, 224–237 (2020a)
Morales, A.J., Reyes, J., Boxx, I., Ahmed, K.A.: The effects of turbulence on the lean blowout mechanisms of bluff-body flames. Proc. Combust. Inst. **3**, 1–9 (2020b). https://doi.org/10.1016/j.proci.2020.06.138
Nair, S., Lieuwin, T.: Near-blowoff dynamics of a bluff-body stabilized flame. J. Propuls. Power. **23**, 421–427 (2007)
Otsu, N.: A threshold selection method from gray-level histograms. IEEE Trans. Syst. Man. Cybern. **9**, 62–66 (1979)
Ozawa, R.I.: Survey of basic data on flame stabilization and propagation for high speed combustion systems. Science **5**, 10 (1971)
Pfadler, S., Beyrau, F., Leipertz, A.: Flame front detection and characterization using conditioned particle image velocimetry. Opt. Express **15**(23), 15444–15456 (2007)
Pope, S.B.: Turbulent Flows. Cambridge University Press, Cambridge (2000)
Reyes, J., Kailasanathan, R.K.A.: Relationship between the chemiluminescence intensity rato of C2* and CH*, charge pressure, and gasoline. Energy Fuels **32**, 10933–10940 (2018)
Roy Chowdhury, B., Cetegen, B.M.: Experimental study of the effects of free stream turbulence on characteristics and flame structure of bluff-body stabilized conical lean premixed flames. Combust. Flame. **178**, 311–328 (2017)
Sardi, K., Whitelaw, J.H.: Extinction timescales of periodically strained, lean counterflow flames. Exp. Fluids. **27**, 199–209 (1999)
Sardi, K., Taylor, A.M.K.P., Whitelaw, J.H.: Extinction of turbulent counterflow flames under periodic strain. Combust. Flame. **120**, 265–284 (2000)
Sciacchitano, A., Wieneke, B.: PIV uncertainty propagation. Meas. Sci. Technol. **27**, 1–16 (2016)
Shanbhogue, S.J., Husain, S., Lieuwen, T.: Lean blowoff of bluff body stabilized flames: scaling and dynamics. Prog. Energy Combust. Sci. **35**, 98–120 (2009)
Skiba, A.W., Carter, C.D., Hammack, S.D., Miller, J.D., Gord, J.R., Driscoll, J.F.: The influence of large eddies on the structure of turbulent premixed flames characterized with stereo-PIV and multi-species PLIF at 20kHz. Proc. Combust. Inst. **37**, 2477–2484 (2019)
Steinberg, A.M., Dirscoll, J.F.: Straining and wrinkling processes during turbulence-premixed flame interaction measured using temporally-resolved diagnostics. Combust. Flame. **156**, 2285–2306 (2009)
Tuttle, S.G., Chaudhuri, S., Kopp-Vaughan, K.M., Jensen, T.R.: Lean blowoff behavior of assymetrically-fueled bluff body-stabilized flames. Combust. Flame. **160**, 1677–1692 (2013)
Welch, P.: The use of fast fourier transform for the estimation of power spectra: a method based on time averaging over short, modifed periodograms. IEEE Trans. Audio Electroacoust. **15**, 70–73 (1967)
Zukoski, E.E., Marble, F.E.: Experiments concerning the mechanism of flame blowoff from bluff bodies. Proc. Gas Dyn. Symp. Aerothermochemistry. **5**, 205–210 (1956)